





## Article

# Topological and Fractal Analysis of Nanostructured Metal–Dielectric Films

Ivan Bolesta <sup>1</sup>, Oleksii Kushnir <sup>1</sup>, Ivan Karbovnyk <sup>1</sup>, Halyna Klym <sup>2,\*</sup>, Marina Konuhova <sup>3</sup> and Anatoli I. Popov <sup>3,\*</sup>

<sup>1</sup> Department of Radiophysics and Computer Technologies, Ivan Franko National University of Lviv, 107 Tarnavskogo Str., 79017 Lviv, Ukraine; ivan.bolesta@lnu.edu.ua (I.B.); oleksiy.kushnir@lnu.edu.ua (O.K.); ivan.karbovnyk@lnu.edu.ua (I.K.)

<sup>2</sup> Department of Specialized Computer Systems, Lviv Polytechnic National University, 12 Bandera Str., 79013 Lviv, Ukraine

<sup>3</sup> Institute of Solid State Physics, University of Latvia, Kengaraga 8, LV-1063 Riga, Latvia; marina.konuhova@cfi.lu.lv

\* Correspondence: halyna.i.klym@lpnu.ua (H.K.); popov@latnet.lv (A.I.P.)

**Abstract:** The surface topology and fractal dimension of ultrathin silver and gold films have been investigated utilizing atomic force microscopy. These films were formed at the early stages of metal deposition through thermal evaporation and have pre-percolation thicknesses. They contain both metallic and insulating (void) phases, making them metal–dielectric composites. We identified the main parameters of the microstructure, such as the size of the metallic particles and surface roughness, as well as the dependence of these parameters on the film thickness and substrate parameters. Approaches to processing data, including correlation analysis, were employed. An analysis of dependencies and an explanation of their appearance were conducted. The discussion also addressed the limitations of using atomic force microscopy for studying ultrathin metal films. We determined the various types of fractal dimensions, considering the film topology for two- as well as three-dimensional objects. Depending on the actual dimensions of the phase boundary for silver films, a maximum was found. Different approaches to determining the fractal dimensions in 3Ds case show a similar dependence, but different values.

**Keywords:** atomic force microscopy; thin films; topology; surface; nanostructures; fractal; percolation



Academic Editors: Wenluan Zhang, Yumin Huang and Pan Liu

Received: 12 February 2025

Revised: 8 March 2025

Accepted: 10 March 2025

Published: 17 March 2025

**Citation:** Bolesta, I.; Kushnir, O.; Karbovnyk, I.; Klym, H.; Konuhova, M.; Popov, A.I. Topological and Fractal Analysis of Nanostructured Metal–Dielectric Films. *Appl. Sci.* **2025**, *15*, 3250. <https://doi.org/10.3390/app15063250>

**Copyright:** © 2025 by the authors. Licensee MDPI, Basel, Switzerland. This article is an open access article distributed under the terms and conditions of the Creative Commons Attribution (CC BY) license (<https://creativecommons.org/licenses/by/4.0/>).

## 1. Introduction

The fast development of industry and technology demands the creation of increasingly novel functional materials with unique properties [1–6]. A major area of emphasis for researchers is the development of more efficient light-emitting or light-absorbing materials [7,8]. Metal–dielectric composites with phases the size of nanometers show promise in this regard [9,10]. These materials’ optical response is mostly determined by the metallic phase characteristics, which means that the response can be controlled by varying the corresponding parameters of metallic nanostructures [11–13]. It was demonstrated [14,15] that the energy redistribution in such materials can lead to the amplification of local optical fields. This effect is linked to the nascency of surface plasmon resonance in metallic nanoparticles as a result of the conduction electrons oscillating inside them [16–18]. Significant local field enhancement occurs in stochastic metal–dielectric structures with randomly distributed metallic nanoparticles of different sizes. A model example of such metal–dielectric

nanostructures is thin metal films produced by thermal evaporation, with thicknesses below the percolation threshold [19–21].

The stochastic creation of metal islands takes place during the initial phases of deposition. The parameters of the structure are determined by the substrate's quality and temperature [22–24], its surfactant sublayers [25,26], and other factors [27–30]. From a practical standpoint, island films of silver (Ag) and gold (Au) are very intriguing since the frequency of the plasmon resonance in such structures falls within the visible and near-ultraviolet ranges [31–34]. Due to the plasmonic effect, nanoparticles of these metals have been applied in various ways, including in solar energy [35,36], in biomedical fields [37,38], and in the creation of new materials [39,40], among others. Consequently, studying the morphology and determining the integral structural parameters of ultrathin gold and silver films is crucial as it directly affects the characteristics of the materials.

The purpose of this work is topological and fractal dimension analysis of ultrathin silver and gold films with thicknesses below the percolation threshold using atomic force microscopy (AFM). The study of surface evolution of films with increasing mass thickness is the basis for determining a set of various parameters, including classical ones such as roughness and grain size, as well as those based on correlation analysis. The probe's influence on the surface image's quality and reliability is also thoroughly analyzed. Various approaches are used in this work to determine the fractal dimensionality, among which the metal film is considered as either a 2D or 3D object.

## 2. Materials and Methods

Ultrathin films of silver and gold were produced by the thermal evaporation of metal in vacuum conditions at a pressure of  $10^{-6}$  torr and a speed of 0.01...0.02 nm/s. Substrates from glass, maintained at a temperature of 290 K, were chosen for this process. Mass thickness  $d_m$  is an important practical parameter of the films, which corresponds to the thickness of a solid, homogeneous metal layer of the same mass as the experimental film. The bulk thickness  $d_m$  of the films was controlled during sputtering using a quartz crystal microbalance. For structural studies, a set of silver films with mass thicknesses between 1.0 and 6.0 nm, significantly below the percolation threshold of approximately 18 to 20 nm, was deposited [41,42]. Gold films were fabricated within the thickness range of 1.0 to 3.0 nm, as films with  $d_m \geq 5.0$  nm transitioned into a percolating state. For some additional studies, samples with larger mass thicknesses were also used, namely 10 nm and 17.8 nm for silver and 4, 6, and 8 nm in the case of gold films. Silver and gold with a purity of 99.99%, obtained from Sigma-Aldrich, were used for thermal evaporation. During metal deposition, island structures are created, presenting with different characteristics depending on the substrate and its temperature. These structures can be called metal–dielectric composites with a fractal order [43].

Morphological analyses of the metallic film surfaces were performed using Solver P47 PRO (NT-MDT) with NSG10 cantilevers possessing a tip curvature radius of 6–10 nm. The studies were conducted in tapping mode, with a scan rate between 0.5 and 2 lines per second (LPS) so as not to damage the surface of the film.

The initial processing and image reconstruction of the AFM data were performed using Gwyddion [44], a freely available and open-source modular software suite under the GNU General Public License. This software is specifically designed for the visualization and analysis of data acquired via scanning probe microscopy (SPM) techniques. Python 3.11 scripts were used all further data processing and parameter determination, such as roughness, particle size, and fractal dimensions. In addition to the implementation of our own algorithms, the scripts also use the NumPy 2.1.0 and OpenCV 3.2 libraries. Gwyddion 2.67 was also used to visualize some resulting surfaces.

### 3. Results and Discussion

The pre-percolation topology of Ag thin films formed on substrates (Figure 1) was studied by atomic force microscopy. Figure 1d indicates the topology of the glass substrate without the applied film. From the comparison of the topologies of the surface of glass and films, it can be seen that the height difference of the glass surface is more than ten times smaller than that corresponding to films, at 3.5 nm versus 35–40 nm. This is because, at such magnifications, the glass has a slowly changing relief, and the inclusions that may be in the glass are huge compared to the size of the silver particles that make up the film. Therefore, for this experiment, the influence of substrate topology is negligible. The mass thickness of the films ( $d_m$ ) was varied to study its effect on surface morphology. It was found that ultrathin films consisted of aggregated metal nanoparticles, with their size and shape being dependent on  $d_m$ . This conclusion aligns with studies conducted using similar methods to obtain metal films on glass substrates under similar conditions [45–49]. Notably, pre-percolation Au films exhibited qualitatively similar surface features to Ag films (Figure 2), although with smaller nanoparticle dimensions.

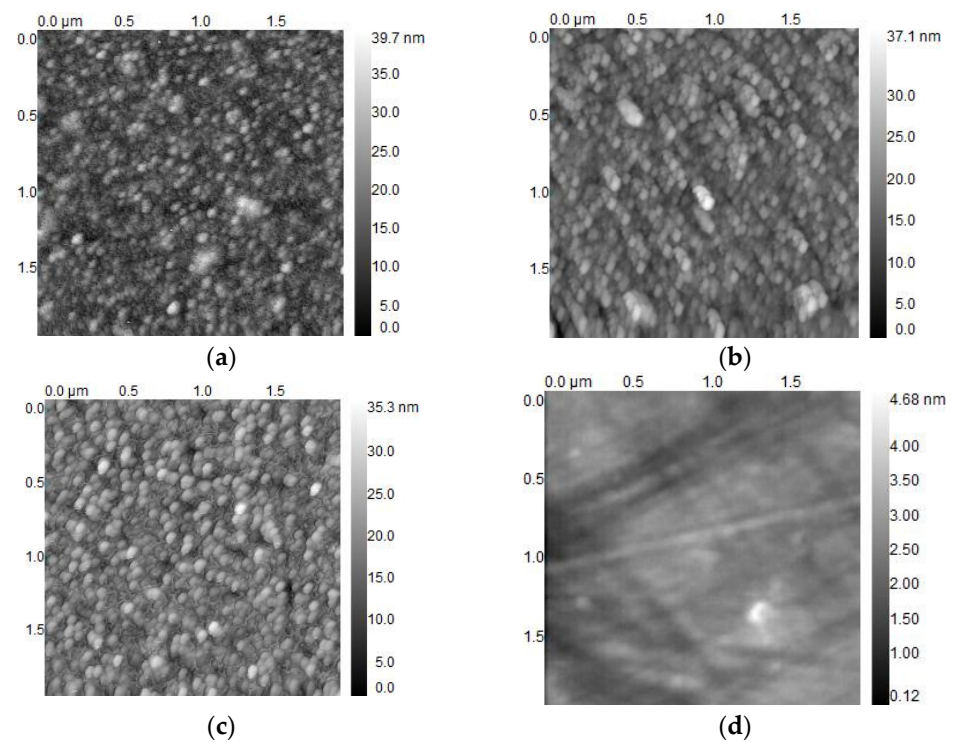


**Figure 1.** AFM visuals of the Ag films on substrates with thicknesses ( $d_m$ ) of 1.1 nm (a), 3.6 nm (b), and 5.7 nm (c), and of the glass substrate without film (d) at dimensions of  $2.0 \times 2.0 \mu\text{m}$ .

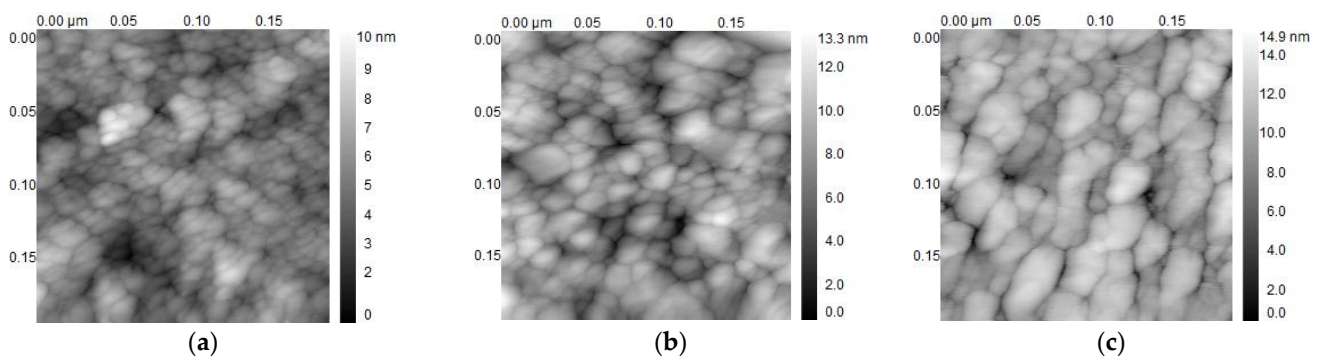


**Figure 2.** AFM visuals of the Au films on substrates with thicknesses ( $d_m$ ) of 1.0 nm (a), 2.0 nm (b), and 3.0 nm (c) at dimensions of  $0.2 \times 0.2 \mu\text{m}$ .

It should be noted that the AFM image dimensions, shown in Figures 1 and 2, are different. This is due to the significant size difference in surface inhomogeneities between silver and gold films. These images are presented to illustrate the structural evolution with the increasing mass thickness of the films. Most parameters were calculated using image sets with different dimensions.

To quantitatively analyze the surface roughness, the root mean square (RMS) deviation of the topography from a reference plane was calculated based on the AFM data. In the case of two dimensions, this parameter represents the minimum RMS deviation and characterizes the overall variation in the surface profile [50]:

$$S_q = \sqrt{\frac{\sum_{i=1}^N (Z_i - Z_c)^2}{N}}, \quad (1)$$

where  $Z_i$  is the point height,  $Z_c$  is the average surface height, and  $N$  signifies the total number of points considered on the surface for calculation.

Figure 3 illustrates how the surface roughness depends on the thickness of the films studied.

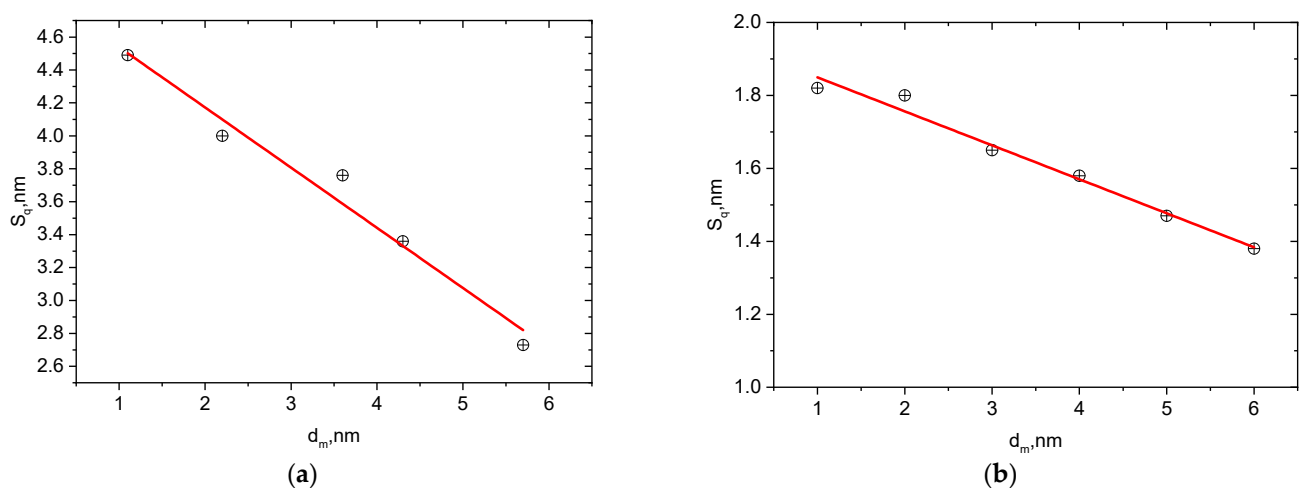


**Figure 3.** The dependence of the surface roughness of Ag (a) and Au (b) films deposited on substrates (depicted on Figure 1d) on mass thickness. Circles—calculated values, red line—linear fitting.

Further analysis of AFM and the objectivity of the parameters that can be obtained with its help is required to understand the reasons for the dependence of RMS on the mass thickness of metal films. Atomic force microscopy is a useful instrument for studying surface topology at the nanoscale [51–53]. The positioning of the probe system relative to the sample enables a fairly accurate reproduction of the surface profile. However, in nanophysics, the objects under study have sizes of tens of nanometers. In this case, the limited size of the scanning probe is a significant drawback and introduces considerable errors in the measurement results [51,52].

According to the principles of operation of a scanning microscope, the signal obtained when scanning a line is a convolution of the surface shapes and the scanning element. It is widely known that mathematically each point of an AFM image can be represented as a part of the convolution of the surface relief signals,  $f(x,y)$ , and the probe shape,  $p(x,y)$  [54]:

$$g(x,y) = \int_0^x \int_0^y f(\xi,\eta) p(x-\xi, y-\eta) d\xi d\eta. \quad (2)$$

When using an atomic force microscope in contact or semi-contact scanning modes, the condition of the minimum distance of the probe from the examined surface will be fulfilled. Mathematically, this condition is written as follows [54]:

$$p(x,y) - f(x,y) \geq 0. \quad (3)$$

Considering these two factors, a simple algorithm for modeling the AFM scanning process was proposed for use if the shape of the probe  $p(x,y)$  and the relief of the real surface  $f(x,y)$  are known. This algorithm is carried out in one: (1) assume that the center of the probe tip is positioned over a given point; (2) the initial height value at this point on the new (modeled) surface is set to be the same as that on the real surface  $f(x,y)$ ; (3) find the maximum difference  $p(x,y) - f(x,y)$  over the entire area of the probe with the center at the given point; (4) if the obtained maximum difference is positive, the height value at this point on the new surface  $g(x,y)$  is increased by the obtained difference value (Figure 4).

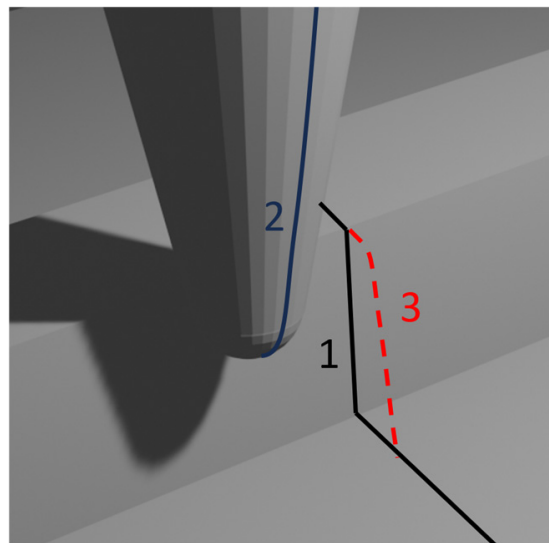


**Figure 4.** Conceptual illustration of AFM scanning procedure. 1— $f(x)$ , the real shape of the surface; 2— $p(x)$ , the shape of the probe; 3— $g(x)$ , the resulting topology.

On the other hand, metal films in the initial stages of sputtering form islands, the shapes of which can be roughly considered spheres or hemispheres depending on the wetting level of the substrate surface by the metal, which, in turn, depends on various thermodynamic parameters. As the amount of metal increases, the islands formed increase in size, and the distance between them decreases, accordingly. Figure 5 is built by analogy with the approach used for the formation of Figure 4. It schematically shows the formation of an AFM image of two spheres in cases when the distance between them is greater (Figure 5a) and less (Figure 5b) than the size of the scanning element. Condition (3) in the case of Figure 4, a does not allow the probe to sink sufficiently to reach the surface of the substrate. From Figure 5, it can be seen that the height  $h_1$  is smaller than  $h$ , and since the distance between the particles decreases with the increase in mass thickness, the roughness decreases.

The influence of the probe on the AFM visuals of island films is more pronounced at the boundary between the 10 nm thick silver film and the glass substrate (Figure 6). To produce these images, several series of experiments were conducted using a sharp tool with a hardness lower than that of glass to scratch the samples' surfaces. By scanning with a gradual increase in scale, an area without debris and with a clear boundary was identified.



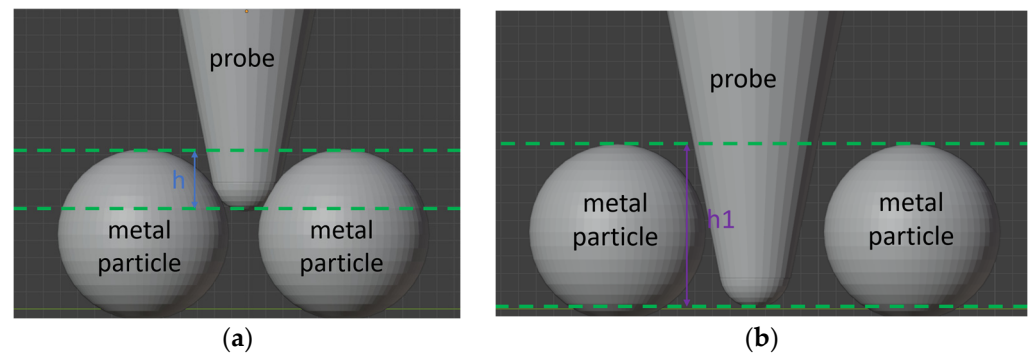


**Figure 5.** The difference between the immersion depth of the probe in the case of two spheres, separated by smaller (a) and larger (b) distances between spheres compared to the size of the probe. The green dash-line indicates the upper and lower limits of the AFM topology that will be obtained in both cases.

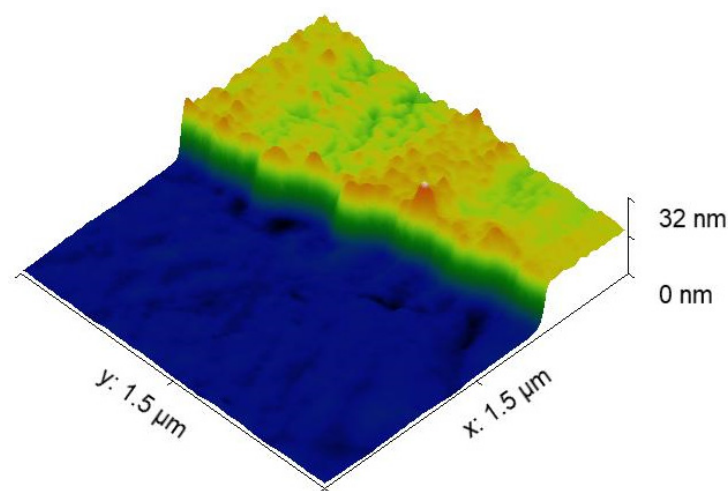


**Figure 6.** A three-dimensional image of the transition boundary between the film and the substrate.

To obtain the image shown in Figure 6, a typical technique for processing AFM data—polynomial background removal—was used. In this case, only the part of the image corresponding to the substrate surface was applied as the basis for calculating the surface parameters.

It is known that such a film is not yet conductive and consists of islands; however, Figure 6 gives the impression that the film is continuous. This representation makes it evident that during the scanning of the film, the probe does not reach the surface of the substrate, but only slightly penetrates it. In this case, the size of the probe affects both the RMS values determined from the AFM images and the estimation of the metal particle sizes.

In both regions depicted in Figure 6, heterogeneity and different surface roughness values can be observed. These areas correspond to the silver film and the glass substrate; direct thickness measurement is not feasible, however. To accurately estimate thickness under these conditions, a height histogram was utilized (Figure 7). In this histogram, the height  $h$  is plotted on the  $x$ -axis, and the point quantity in the AFM image at that height is plotted on the  $y$ -axis. The histogram exhibits two distinct peaks. The left peak is attributed to the substrate, whereas the right peak corresponds to the film surface. Both surfaces exhibit Gaussian distributions, allowing these peaks to be fitted with Gaussian peak functions to determine the positions of their centers, representing the most probable height of the given area. The distance between the centers of these peaks corresponds to the desired geometric thickness  $\delta$  of the metal layer on the substrate.

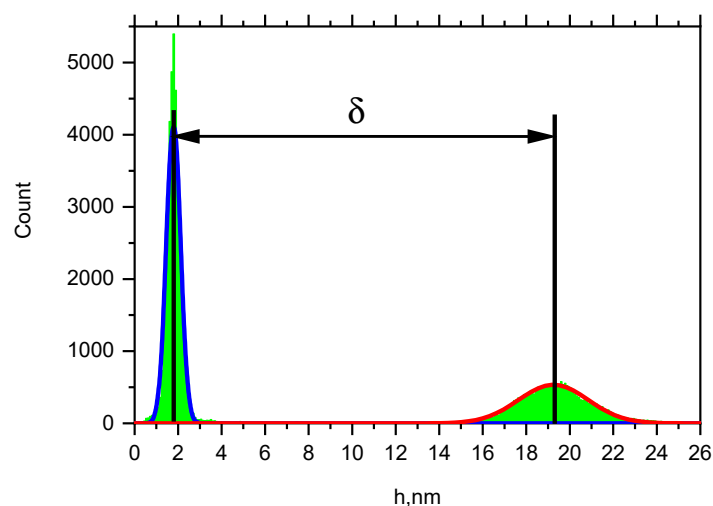


**Figure 7.** A histogram of the height distribution of image points (Figure 6) for the film–substrate transition boundary (green columns) and the approximation of each of the maxima of the distribution by Gaussian functions (blue and red solid lines).

This technique enabled the accurate estimation of the geometric thickness of the film, contingent on identifying the transition limit. The digital processing of the AFM image in the area where the boundary between the film surface and the substrate is visible allows us to determine the spatial thickness of the film layer. Figure 8 illustrates the relationship between the geometric thickness of silver films, as determined from a series of AFM experiments, and their mass thickness.

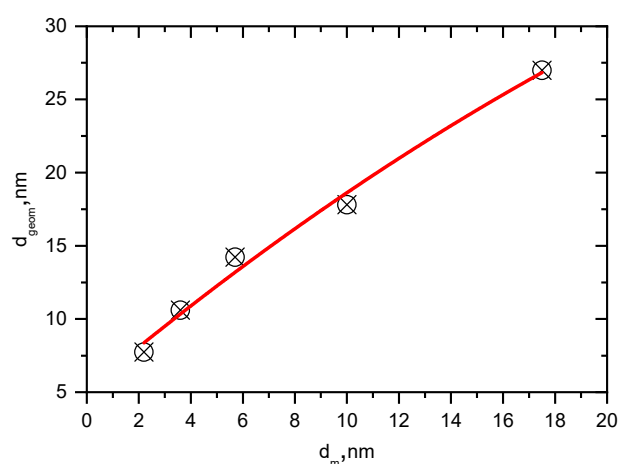


**Figure 8.** The dependence of the geometric thickness of the film  $d_{geom}$  on the mass thickness  $d_m$  for Ag films (symbols) and its fitting (red line).

In cases of small mass thicknesses, the difference between  $d_{geom}$  and  $d_m$  is significant. This discrepancy arises because, at the initial stages of deposition, separate metal clusters form, resulting in large  $d_{geom}$  values. As the film thickness further increases, the difference between them should decrease, and so the dependence Figure 8 has a nonlinear character. With both the geometric thickness  $d_{geom}$  and the mass thickness  $d_m$  known, determining the filling factor  $p$  is straightforward. The packing factor, representing the position of the film's volume utilized by the metal, is computed as a ration of the mass thickness  $d_m$  to the geometric thickness  $d_{geom}$  obtained from AFM images. Figure 9 displays the relationship between the filling factor of the metallic phase  $p$  and the mass thickness.

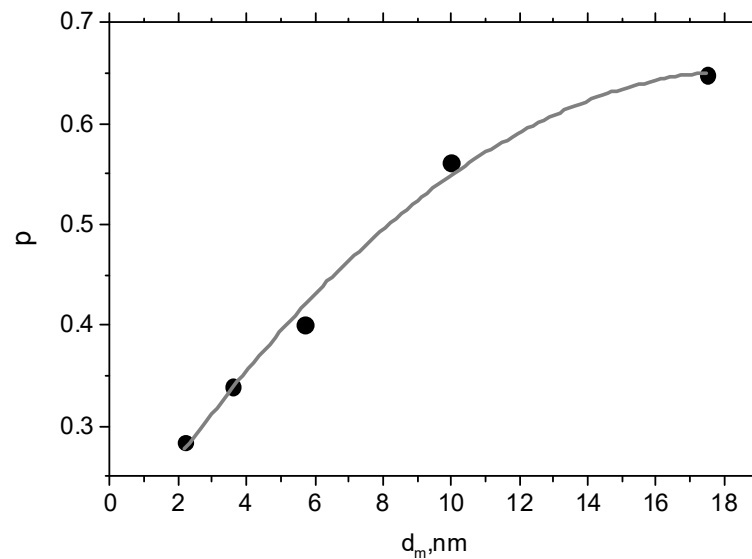


**Figure 9.** Variation in the metal phase filling (packing) factor with the mass thickness of Ag films on a glass substrate.

As expected, the filling factor increases nonlinearly with the increase in mass thickness and asymptotically approaches a value of one for bulk samples.

A different approach was utilized to determine RMS and another surface parameter—the correlation length. The two-dimensional autocorrelation function (ACF) serves as a valuable tool for characterizing the statistical properties of a surface. For stationary surfaces, the following relationship was calculated [55]:

$$C(x, y) = \frac{1}{S} \int_S z(x', y') z(x' + x, y' + y) dx' dy', \quad (4)$$

where  $S$  is the scanning area and  $z(x, y)$  is the AFM topology height.

The following equation can be applied to numerically calculate the correlation function [46]:

$$C(x, y) = F^{-1} \left[ F^{-1} [z(x, y)] F[x, y] \right], \quad (5)$$

where the discrete Fourier transforms, both in reverse and direct, are denoted by  $F^{-1}$  and  $F$ , respectively.

The correlation function for the Gaussian distribution is expressed as follows [55]:

$$C(x, y) = \delta^2 e^{\left(-\frac{x^2 + y^2}{\sigma^2}\right)} \quad (6)$$

where the parameter  $\delta$  corresponds to the surface roughness, and  $\sigma$  is called the correlation length.

Figures 10 and 11 depict the 2D autocorrelation functions of the surface topography for the Ag and Au films studied, respectively. The intersection of these ACFs with the  $y = 0$  plane is also presented. The calculated ACFs reveal an anisotropic character in the cross-sections. While isotropy in the  $xy$ -plane implies a symmetrical correlation function, the observed anisotropy is likely caused by the elongated shape and, to some extent, the preferential orientation of the metallic nanoparticles.



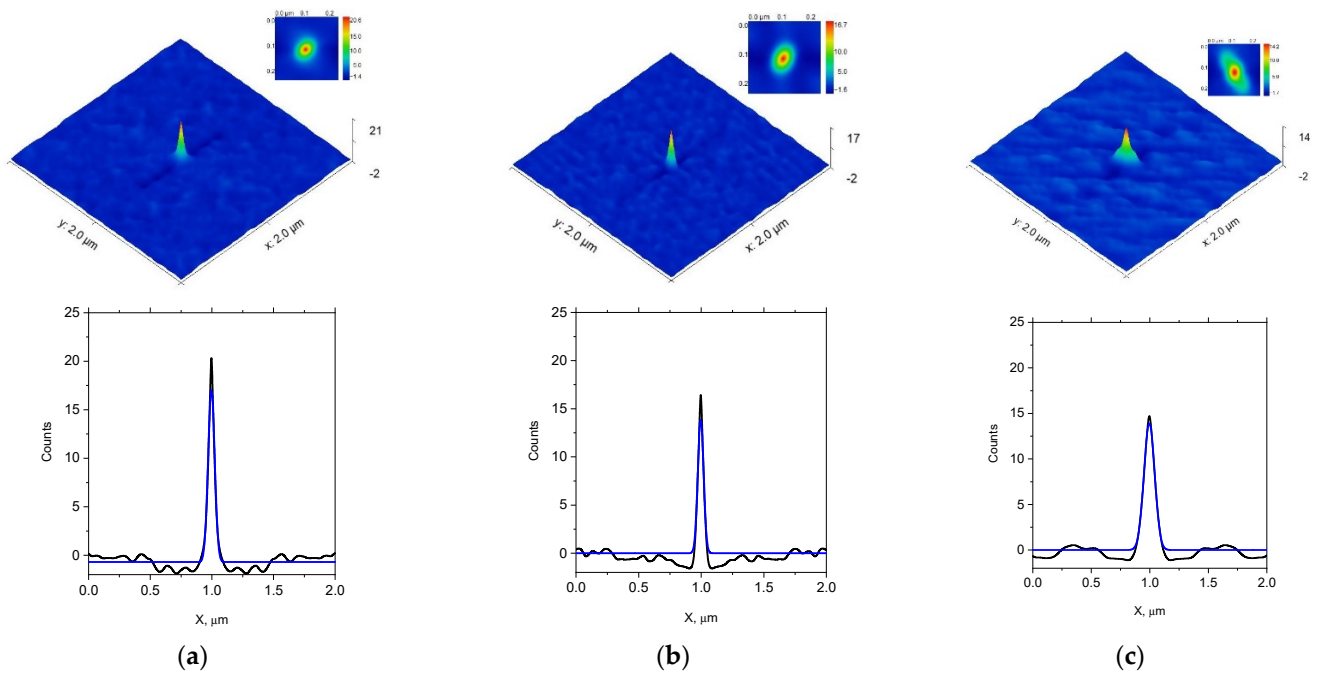


**Figure 10.** The two-dimensional autocorrelation of the surface morphology of the studied Ag films at 1.1 nm (a), 3.6 nm (b), and 5.7 nm (c) mass thicknesses. Additionally, vertical cross-sections along the  $x$ -direction (black line), with corresponding Gaussian fits (blue line) displayed, are included.

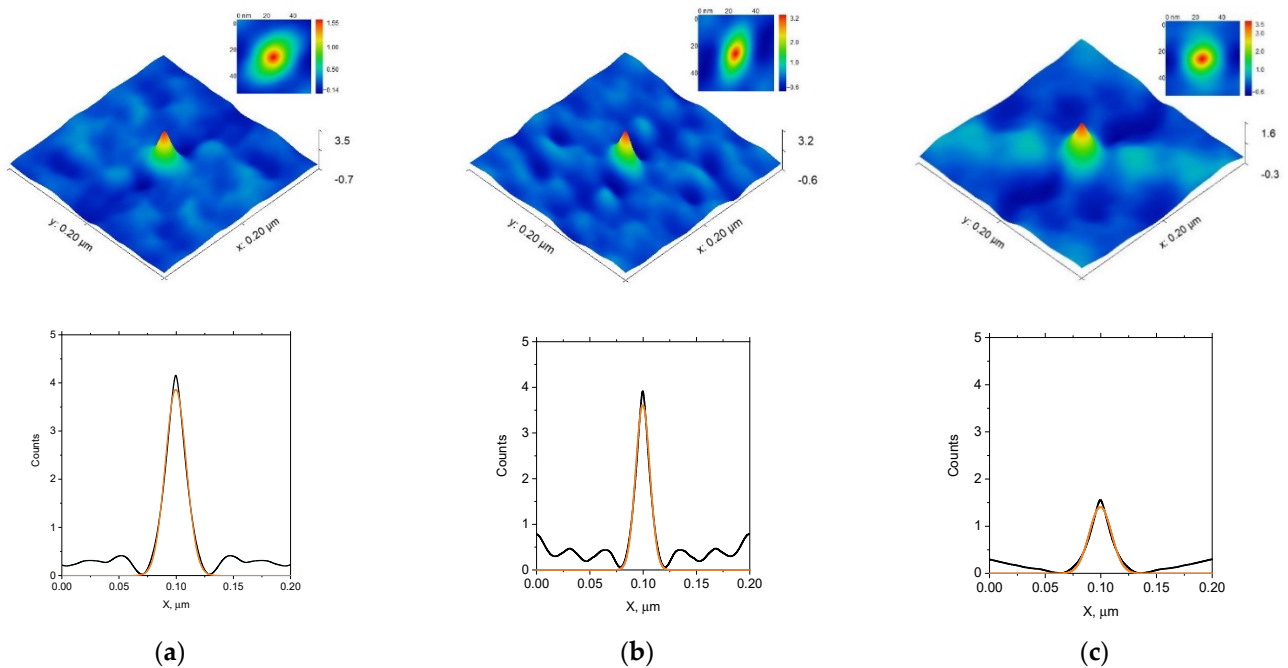


**Figure 11.** The two-dimensional autocorrelation of the surface morphology of the studied Au films at 1.0 nm (a), 2.0 nm (b), and 3.0 nm (c) mass thicknesses. Additionally, vertical cross-sections along the  $x$ -direction (black line), with corresponding Gaussian fits (red line) displayed, are included.

However, according to (2), the shape of the probe  $p(x)$  can affect the surface correlation function's anisotropy. To test this, the shape profiles of the probe tip were determined by scanning a 17 nm high rectangular grating. Figure 12 shows the profiles obtained when scanning at different angles, with a difference of 90 degrees. The difference between the profiles cannot affect the anisotropy of the correlation function, as it is not essential.

Consequently, the anisotropy of the correlation function leads to the conclusion of the anisotropic morphology of nanoparticles.

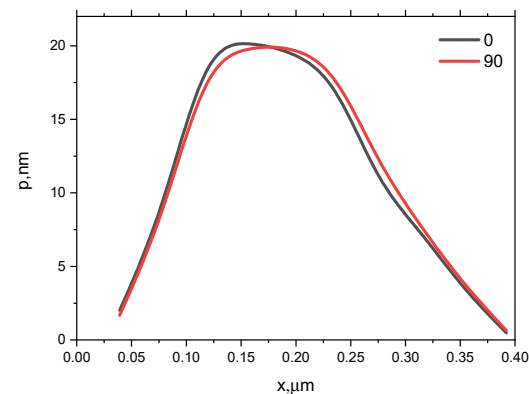


**Figure 12.** Probe tip profiles obtained by scanning 17 nm high rectangular grating at different angles.

The dependence of roughness ( $\delta$ ) and correlation length ( $\sigma$ ) on mass thickness ( $d_m$ ) demonstrates similar trends for both Ag and Au films. An increase in  $d_m$  leads to an expansion of the correlation length paired with a reduction in roughness. Notably, the  $\sigma$  and  $\delta$  values for Au films are consistently 2 to 2.5 times smaller compared to those of Ag films. This disparity can be related to the intrinsically smaller dimension of the Au particles.

The explanation for the decrease in roughness remains consistent, while the increase in correlation length with the increase in mass thickness arises from the growth and merger of metal nanoparticles. Evaluating roughness and conducting correlation analysis enable the assessment of surface statistical characteristics. However, understanding the size of the structural elements is also crucial.

On the other hand, information about the probe's shape (Figure 12) makes it possible to use the deconvolution method [51–53] to partially eliminate the effect that occurs due to the probe's finite size (Figure 4). This method, of course, does not make it possible to completely eliminate the influence of the probe on the shape of the AFM surface, especially in the case of Figure 5a. However, the deconvolution method effectively reduces the error in determining the horizontal dimensions of objects. A change in the appearance of the surface is presented for demonstration: the surface of an ideal sphere if the probe size were infinitely small (Figure 13a), the sphere after the scanning process as in Figure 4 (Figure 13b), and the surface after using deconvolution (Figure 13c).

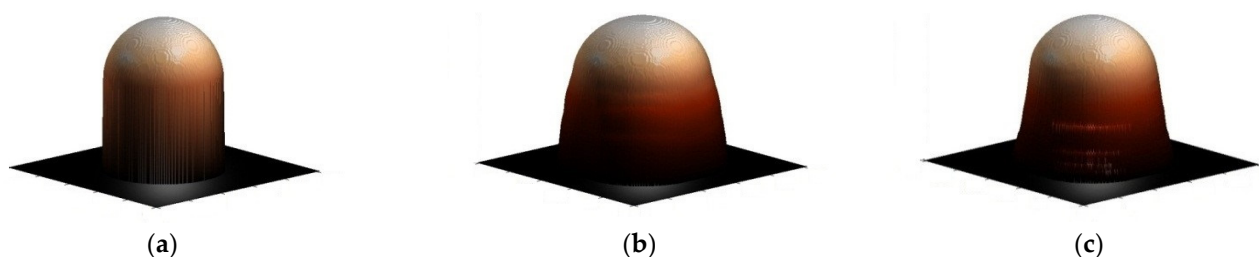


**Figure 13.** The model of an ideal AFM surface of a sphere (a), the surface of a sphere modeled according to the algorithm Figure 4 (b), and the appearance of the surface after using deconvolution (c).

The object size still has an error after using horizontal deconvolution, but it is much closer to the values obtained by other, often more accurate methods [56]. Therefore, the determination of particle sizes according to the following algorithms was carried out after using the de-convolution method for the corresponding AFM images.

The data underwent several processing stages to identify regions in the AFM image corresponding to metal particles. The primary objective was to delineate the contours of these particles. Initially, the image was segmented using the watershed method [57], followed by automatic image thresholding using Otsu's method [58], which was performed on the resulting segments. Subsequently, contours were detected on the binary images obtained. This approach helped mitigate errors arising from unstable height variations in AFM images.

After identifying the boundaries of particles in the image, parameters describing their shape and size were determined. The primary parameter is the region area  $S$  related to each particle. The number  $N$  of image points enclosed by the contour was counted, yielding  $S = N\Delta x\Delta y$ , where  $\Delta x$  and  $\Delta y$  are the discretization steps along the  $x$  and  $y$  axes, respectively. From the area  $S$ , the equivalent diameter  $d_{eq}$  of the particle is derived. This is the diameter of a circle whose area matches the particle's area  $S$ , i.e.,  $d_{eq} = \sqrt{4S/\pi}$ .

The height  $h$  of the particle is determined by finding the maximum  $z_{max}$ , and minimum  $z_{min}$ , height values in the area where the particle appears on the image:  $h = z_{max} - z_{min}$ .

The length  $L$  is different in comparison with the maximum distance among two points within the region, while width  $w$  is not necessarily the minimum distance between two boundary points on opposite sides and is only accurate for convex regions. The same approach was employed as in [59] to determine these parameters: a rectangle with the minimum area enclosing the region was described, where the width of this rectangle was taken as the width of the region, and the length of the rectangle was the length of the region. This method also allows us to estimate the direction of the metal particle with respect to the  $x$ -axis of the image, which corresponds to the orientation (angle  $\varphi$ ) of the longer side of the rectangle.

Figure 14a presents the dependencies of the mean (average) equivalent diameter ( $d_{eq}$ ) of films on the time of deposition at a rate of 0.0016 nm/s. Figure 14b shows the subsection of the same  $d_{eq}$  parameter, but after it has affected the temperature of the substrate at a constant  $d_m$ . It was determined that the increase in  $d_{eq}$  with the rising deposition time  $t$  is nearly linear during the initial deposition stages.

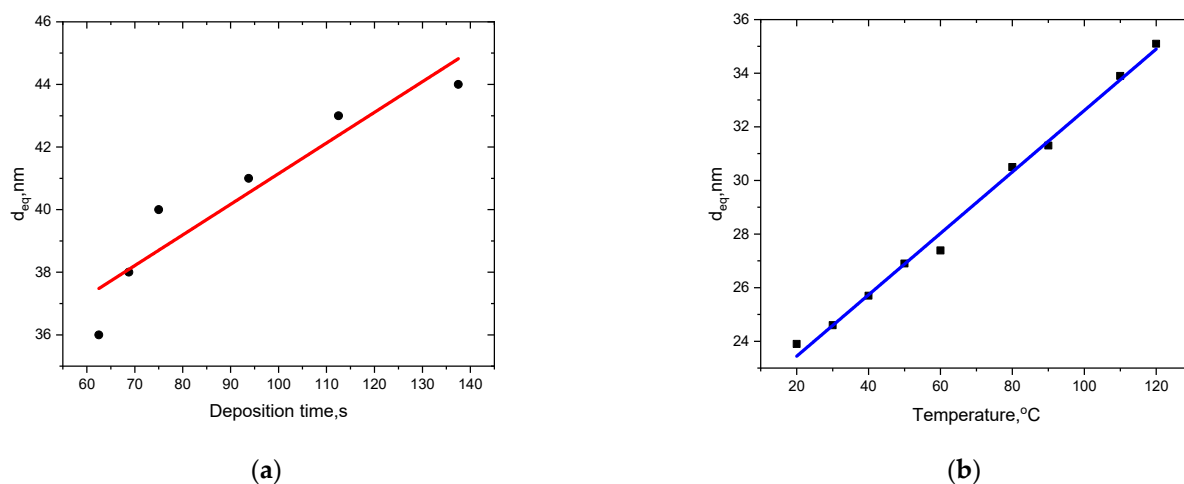


**Figure 14.** Mean (average) particle diameter  $d_{eq}$  for Ag films formed on the substrate at constant  $T = 293$  K vs. deposition time (a) and at a constant thickness of  $d_m = 6$  nm, and the substrate temperature (b).

It is noticed that there is a linear relationship between the characteristic structure size and the substrate temperature  $T$ . This trend can be attributed to the metal particle's enhanced thermal energy  $kT$  at higher temperatures. This increased energy facilitates surface mobility, enabling particles to coalesce and form biggest clusters.

It was demonstrated that, at a low thickness, the metal particle can be modeled in the form of ellipsoids with the sizes of  $a = L$ ,  $b = w$ , and  $c = 2h$  ( $L$  is the length,  $w$  is the width of the area,  $h$  is the elevation above the watershed). The values obtained are displayed in Table 1. Anisotropy in the  $xy$  plane is evident, as indicated by the significant difference between the dimensions of the  $a$  and  $b$  axes and the uneven distribution of particles in the visible region. This can be seen better when the particle distribution is along a certain direction because anisotropy occurs when there is simultaneous particle elongation and non-uniform distribution in the same direction.

**Table 1.** The averaged values of the axes of metal particles for silver films of different mass thicknesses for different images of the same sample.

$d_m (\pm 0.1), \text{ nm}$	$a (\pm 2), \text{ nm}$	$b (\pm 2), \text{ nm}$	$c (\pm 1), \text{ nm}$
1.0	40	30	31
1.1	45	32	32
1.2	47	33	32
1.5	49	33	35
1.8	53	34	34

Combining methods to identify structural components and determine parameters allows for the precise characterization of each particle's geometry individually. The method for defining the area surrounding each particle makes it possible to evaluate both its geometric parameters and its alignment with the  $x$  and  $y$  axes along the rectangle's longest side. This enables the determination of mean values, as well as distributions for the parameters obtained, given an adequate particle number in the collection of visuals for the same sample.

Figure 15 displays the topography of the Ag film's surface at 1.1 nm, with a colored mask applied to the picture and dispensation by equivalent diameters and via the particle's direction. The angle  $\phi$  amid the particle's lateral axis and the positive orientation of the  $x$ -axis specified the orientation of the particles.

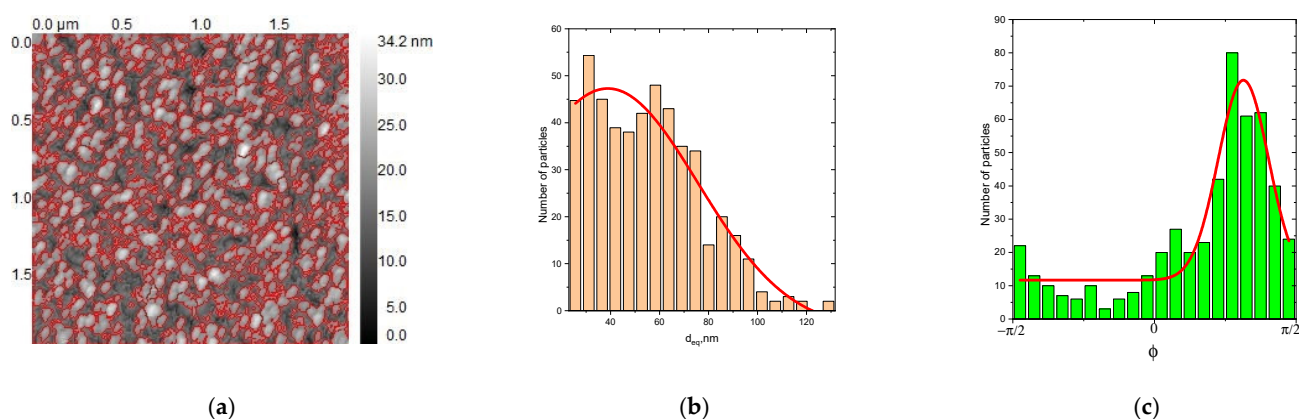


**Figure 15.** Marked metal particles on the AFM image of the Ag film surface  $d_m = 1.1 \text{ nm}$  (a), distributions of the number of particles from the equivalent diameter (b), and the orientation of longest side (c) in relation to the  $x$ -axis of the image.

The distribution of diameters (Figure 15b) shows a Gaussian shape, with a peak in the region of the average diameter. A similar pattern is observed in different images of all samples. The distribution of particle orientations is non-uniform, showing a significant peak, while other orientations exhibit non-zero values. This observation confirms previous findings of a partially uniform orientation of nanoparticles, deduced from the elliptical

cross-section of the auto-correlative function. It is noteworthy this allocation is not typical of all films and can be related to the production technology used.

The determination of the fractal dimensions of the studied films is crucial, as metal–dielectric composites are well established to possess a fractal structure. In this study, the fractal dimension, known as the Hausdorff dimension, was defined using the box-counting method.

In a 2D context, the fractal dimension of metallic phase ( $D_p$ ) can be differentiated from the fractal dimension of the boundaries between the metal and dielectric ( $D_b$ ) using the box-counting approach. When determining  $D_p$ , boxes cover the complete area corresponding to the particles in the picture. A box is considered to cover the area if it contains at least one pixel within the particle region. In contrast, when measuring  $D_b$ , only the boxes intersected by the particle's boundary are considered. This means each box must contain a minimum of one pixel on the boundary line.

Figures 16 and 17 depict the dependencies of the 2D fractal dimensions  $D_p$  for the metal phase  $D_b$  and for the metal–dielectric boundaries of silver and gold films deposited on the substrate as a function of mass thickness.

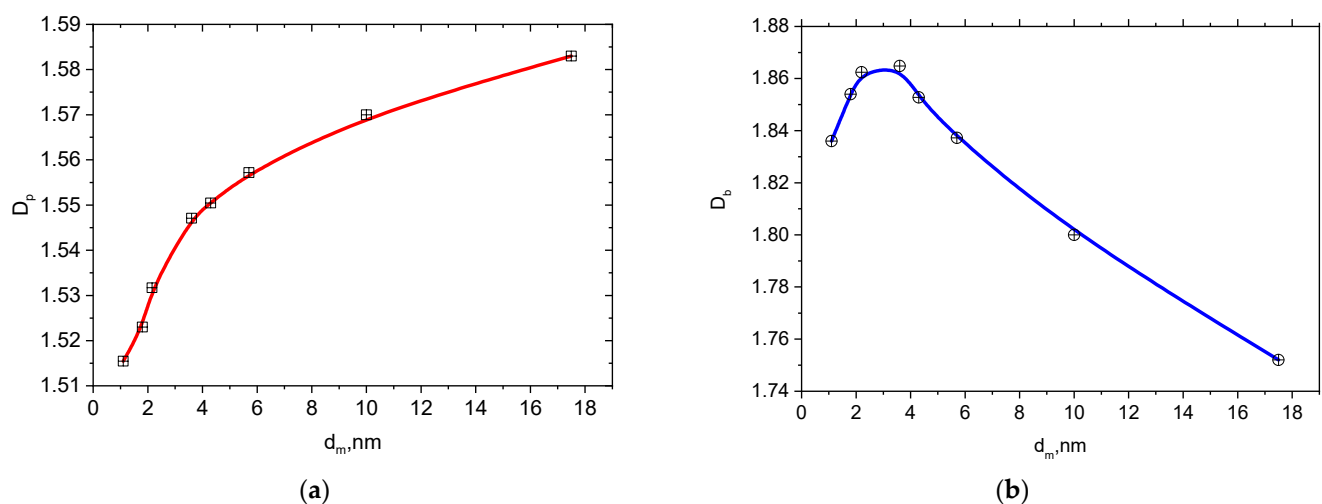


**Figure 16.** Dependencies on the mass thickness of Ag films for the metal phase (a), and the metal–dielectric boundary (b).

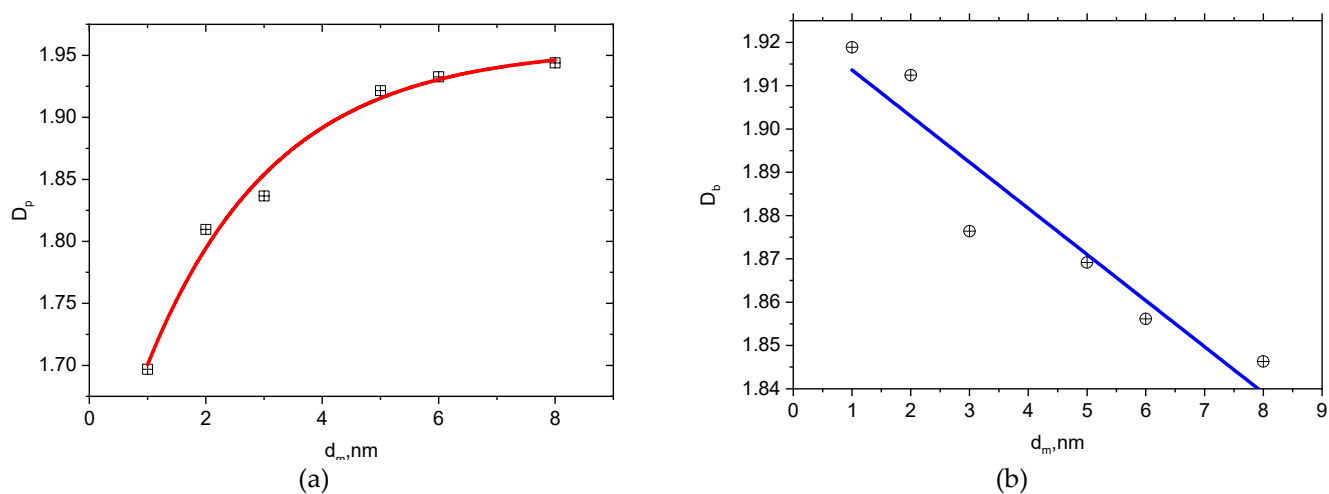


**Figure 17.** Dependencies on the mass thickness of Au films for the metal phase (a) and the metal–dielectric boundary (b).

The fractal dimension  $D_p$  of the metallic phase of both Ag and Au films demonstrates a positive correlation with rising mass thickness. Such a trend can be related to the growing metal content as the film thickness increases, leading to more extensive metal phase filling of the surface.

In contrast, the fractal dimension of the metal–dielectric boundary  $D_b$  exhibits a distinct peak at  $d_m \approx 3$  nm in the case of Ag films. Such behavior can be elucidated by the elongation of the boundary, given that the metal concentration is amplified during the initial stages of deposition. When areas of metal and dielectric parts are proportionally balanced (with a metal filling  $p \approx 0.5$ ), the boundary length reaches its maximum value. With further increases in mass thickness, the boundary length decreases.

In contrast, there is no distinct peak in the  $D_b$  dependence in the case of Au films (Figure 17b), and the dependence on  $D_b$  by  $d_m$  has a decreasing character over the entire range. This suggests that the metal concentration in the studied films exceeds the critical level, which would maximize the boundary length.

In the three-dimensional case, the film surface is described by a height function  $z(x, y)$ . Then, the fractal dimension can be determined by covering the surface with three-dimensional boxes. However, the correlation dimension is more commonly considered for such analysis.

The Wiener–Khinchin theorem [60] establishes a link between the autocorrelation function and the spectral power density. This connection allows us to infer the fractal nature of the surface topography from its power spectrum. Reference [61] demonstrates that the power spectrum of a fractal surface follows a power-law relationship for spatial frequencies:

$$S(\nu_x) = \frac{K_\alpha}{\nu_x^\alpha}, \quad (7)$$

where  $K_\alpha$  represents the spectral strength and  $\alpha$  signifies the spectral index. These parameters are considered fractal characteristics that define surface roughness in the spatial frequency domain. As evident from the equation, the value of  $\alpha$  can be determined from the slope observed in a double logarithmic representation of the power spectrum.

The Blackman–Tuke method [62] is employed to calculate the power spectrum in one dimension as a function of spatial frequencies, as presented in Figure 18 using a double logarithmic scale. The spatial index  $\alpha$  was obtained as 2.52 by fitting these data with a linear model (solid curve).

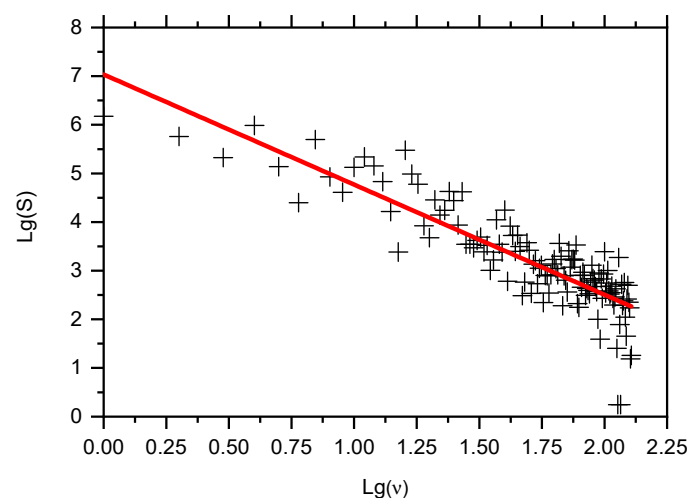


**Figure 18.** Relationship between spectral power (crosses) and spatial frequencies on a double logarithmic scale. The solid line represents the linear fitting of the data points.



The relationship between the  $\alpha$  and  $H$  is provided by  $\alpha = 2H + 1$  [63]. Furthermore, the correlation fractal irregularity  $D_c$  is associated with the fractal co-dimension by the equation  $D_c = 3 - H$  [61].

Figure 19 depicts dependencies of the Hausdorff fractal dimension ( $D_H$ ), assessed using the box-counting approach, as well as correlation dimension ( $D_c$ ) on mass thickness for both Ag and Au films. Each data point represents the average value calculated from the smallest five AFM visuals of the corresponding samples. It was shown that the  $D_c$  consistently remained lower than  $D_H$  ( $D_c < D_H$ ) for both Ag and Au films within the investigated thickness range. It is noteworthy that the rate of change of these fractal dimensions changes as the thickness of the mass increases. In the case of Ag films, the increase is  $0.028 \text{ nm}^{-1}$  for  $D_H$  and  $0.008 \text{ nm}^{-1}$  for  $D_c$ . Similarly, Au films exhibit an increase of  $0.047 \text{ nm}^{-1}$  for  $D_H$  and  $0.027 \text{ nm}^{-1}$  for  $D_c$ .

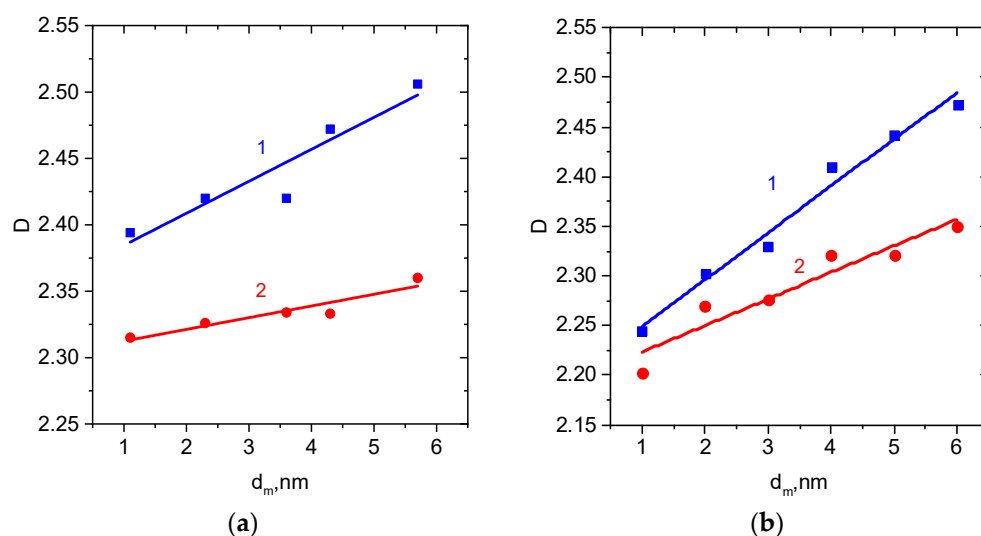


**Figure 19.** Dependencies of the Hausdorff fractal dimension (blue curve 1), and fractal dimension (red curve 2) on  $d_m$  for Ag (a) and Au (b) films.

The observed inequality ( $D_c < D_H$ ) arises from the inherent definitions of these dimensions. The correlation dimension is defined by the following equation [61]:

$$D_q = \lim_{r \rightarrow 0} \frac{1}{q-1} \frac{\ln \sum_k p_k^q}{\ln r}, -\infty \leq q \leq \infty \quad (8)$$

where the summation extends over all boxes of size  $r$  that partition the space, and  $p_k$  represents the probability of particle fractal structure occupying to the  $k$  box. When  $q$  approaches zero ( $q \rightarrow 0$ ), this equation reduces to the dimension determined by the box-counting approach (Hausdorff dimension). In this case, boxes with at least one fractal point are considered during the summation.

Studied correlation dimension relates to a specific value of  $q$  equal 2 ( $D_c = D_2$ ). Due to  $D_q \geq D_{q'}$  for  $q' \geq q$  of multiple distinct fractal dimensions, ( $D_H$  and  $D_c$ ) signify the multifractal nature of the ultrathin film structures.

## 4. Conclusions

Pre-percolation silver and gold films, formed by thermal evaporation at the initial deposition stages, consist of discrete metal particles. AFM effectively studies the topology of these structures, but significant errors occur as films approach percolation, where the distances between metal particles become smaller than the probe tip size. A decrease in surface roughness indicates this and is further supported by examining the film–substrate

border. For much thinner films, such errors are negligible, making AFM-determined parameters reliable. The average particle sizes for silver films with a mass thickness of up to 2 nm range from 30 to 60 nm.

Correlation analysis of film topologies provides further insights into structures. The increase in correlation length with mass thickness and the anisotropy of the central peak of the autocorrelation function indicate growth in the size of surface inhomogeneities (metal particles) and some heterogeneity in their shape and size.

Detailed analysis of the size and shape of silver particles for films with a mass thickness from 1 to 2 nm, performed using image processing, indicates that mainly elliptical particles are formed. The average length and width of these particles increase with the growth of mass thickness, ranging from 43 to 56 nm and from 31 to 36 nm, respectively. Studies also reveal that particle size increases with the substrate temperature during metal deposition. This could be due to the faster crystallization of the metal at lower temperatures, leading to the creation of larger amounts of smaller particles.

The different approaches used in this study to determine fractal dimensionality generally yield predictable results. The fractal dimensionality of the metallic phase asymptotically approaches 2 with increasing mass thickness. However, the peak in the fractal dimensionality of the boundary at  $d_m \sim 3$  nm can indicate a maximum in the boundary length between metal and voids, suggesting that there is a metal filling factor of around 0.5 at this thickness. Contrarily, based on the film–substrate boundary examination, the metal filling factor should be 0.5 at approximately  $d_m \sim 7$  nm. This discrepancy is likely due to errors introduced by the AFM probe.

**Author Contributions:** Conceptualization, I.B.; methodology, I.K.; software, O.K.; validation, I.K., M.K. and H.K.; investigation, O.K.; writing—original draft preparation, O.K. and H.K.; writing—review and editing, O.K., H.K., I.B., I.K. and A.I.P.; data curation, O.K., H.K., M.K. and I.K.; project administration, I.B. and A.I.P. All authors have read and agreed to the published version of the manuscript.

**Funding:** This research was funded by the Ministry of Education and Science of Ukraine (Project “Multisensor robotic systems using nanomaterials to enhance defense capability and safety in emergency situations”). In addition, the research of M.K. and A.I.P. was partly supported by COST Action CA20129 “Multiscale Irradiation and Chemistry Driven Processes and Related Technologies” (MultiChem) and by HORIZON 2020 RISE-RADON Project “Irradiation driven nanofabrication: computational modelling versus experiment”.

**Data Availability Statement:** The data presented in this study are available on request from the corresponding author.

**Acknowledgments:** H.K. and O.K. are grateful for the support from the Education and Science of Ukraine (Project “Multisensor robotic systems using nanomaterials to enhance defense capability and safety in emergency situations”).

**Conflicts of Interest:** The authors declare no conflicts of interest.

## References

1. Niguma, R.; Matsuyama, T.; Wada, K.; Okamoto, K. Novel Plasmonic Metamaterials Based on Metal Nano-Hemispheres and Metal-Dielectric Composites. *Photonics* **2024**, *11*, 356. [\[CrossRef\]](#)
2. Ren, J.; Liang, D.; Liu, H.; Yang, Y.; Li, A.; Sun, Y.; Wang, C. High-temperature thermal stable solar selective absorbing coating based on the dielectric-metal-dielectric structure. *Mater. Today Phys.* **2023**, *34*, 101092. [\[CrossRef\]](#)
3. Klym, H.; Karbovnyk, I.; Piskunov, S.; Popov, A.I. Positron annihilation lifetime spectroscopy insight on free volume conversion of nanostructured  $\text{MgAl}_2\text{O}_4$  ceramics. *Nanomaterials* **2021**, *11*, 3373. [\[CrossRef\]](#)
4. Karbovnyk, I.; Borshchyshyn, I.; Vakhula, Y.; Lutsyuk, I.; Klym, H.; Bolesta, I. Impedance characterization of  $\text{Cr}^{3+}$ ,  $\text{Y}^{3+}$  and  $\text{Zr}^{4+}$  activated forsterite nanoceramics synthesized by sol–gel method. *Ceram. Int.* **2016**, *42*, 8501–8504. [\[CrossRef\]](#)

5. Nur-E-Alam, M.; Basher, M.K.; Vasiliev, M.; Das, N. Physical vapor-deposited silver (Ag)-based metal-dielectric nanocomposites for thin-film and coating applications. *Appl. Sci.* **2021**, *11*, 6746. [\[CrossRef\]](#)
6. Klym, H.; Ingram, A.; Shpotyuk, O.; Karbovnyk, I. Influence of CsCl addition on the nanostructured voids and optical properties of 80GeS<sub>2</sub>-20Ga<sub>2</sub>S<sub>3</sub> glasses. *Opt. Mater.* **2016**, *59*, 39–42. [\[CrossRef\]](#)
7. Wang, W.; Qi, L. Light management with patterned micro-and nanostructure arrays for photocatalysis, photovoltaics, and optoelectronic and optical devices. *Adv. Funct. Mater.* **2019**, *29*, 1807275. [\[CrossRef\]](#)
8. Cheng, P.; An, Y.; Jen, A.K.Y.; Lei, D. New Nanophotonics Approaches for Enhancing the Efficiency and Stability of Perovskite Solar Cells. *Adv. Mater.* **2024**, *36*, 2309459. [\[CrossRef\]](#)
9. Nur-E-Alam, M.; Lonsdale, W.; Vasiliev, M.; Alameh, K. Application-Specific oxide-based and metal–dielectric thin-film materials prepared by radio frequency magnetron sputtering. *Materials* **2019**, *12*, 3448. [\[CrossRef\]](#)
10. Chlebus, R.; Chylek, J.; Ciprian, D.; Hlubina, P. Surface plasmon resonance based measurement of the dielectric function of a thin metal film. *Sensors* **2018**, *18*, 3693. [\[CrossRef\]](#)
11. Willey, R.R.; Stenzel, O. Designing optical coatings with incorporated thin metal films. *Coatings* **2023**, *13*, 369. [\[CrossRef\]](#)
12. Kravets, V.; Poperenko, L.; Kudryavtsev, Y.; Kovanzhi, P. Optical properties and electron characteristics of noble-metal-dielectric oxide nanostructures with covered graphene layer. *Opt. Mater. X* **2023**, *19*, 100256. [\[CrossRef\]](#)
13. Eldabagh, N.; Micek, M.; DePrince, A.E., III; Foley, J.J., IV. Resonance Energy Transfer Mediated by Metal–Dielectric Composite Nanostructures. *J. Phys. Chem. C* **2018**, *122*, 18256–18265. [\[CrossRef\]](#)
14. Yue, D.; Zhang, W.; Wang, P.; Zhang, Y.; Teng, Y.; Yin, J.; Feng, Y. Constructing asymmetric gradient structures to enhance the energy storage performance of PEI-based composite dielectrics. *Mater. Horiz.* **2024**, *11*, 726–736. [\[CrossRef\]](#) [\[PubMed\]](#)
15. Ge, S.; Liu, S.; Feng, W.; Bao, Z.; Liu, Y.; Xue, Y.; Cheng, B. Achieving high energy storage performance and thermal stability concurrently in the cost-cutting Al<sub>2</sub>O<sub>3</sub>/Ba<sub>0.6</sub>Sr<sub>0.4</sub>Ti<sub>0.95</sub>Ce<sub>0.05</sub>O<sub>3</sub>/ZrO<sub>2</sub> composite films for energy storage applications. *Ceram. Int.* **2023**, *49*, 9155–9164. [\[CrossRef\]](#)
16. Katyal, J.; Badoni, V. Localized surface plasmon resonance and field enhancement of Au, Ag, Al and Cu nanoparticles having isotropic and anisotropic nanostructure. *Mater. Today Proc.* **2021**, *44*, 5012–5017. [\[CrossRef\]](#)
17. Coello, V.; Abdulkareem, M.U.A.; Garcia-Ortiz, C.E.; Sosa-Sánchez, C.T.; Téllez-Limón, R.; Peña-Gomar, M. Plasmonic Coupled Modes in a Metal–Dielectric Periodic Nanostructure. *Micromachines* **2023**, *14*, 1713. [\[CrossRef\]](#)
18. Gentile, A.; Ruffino, F.; Grimaldi, M.G. Complex-morphology metal-based nanostructures: Fabrication, characterization, and applications. *Nanomaterials* **2016**, *6*, 110. [\[CrossRef\]](#)
19. Gompf, B.; Dressel, M.; Berrier, A. Impedance spectroscopy and equivalent circuits of metal-dielectric composites around the percolation threshold. *Appl. Phys. Lett.* **2018**, *113*, 243104. [\[CrossRef\]](#)
20. Chen, H.; Wang, F.; Li, K.; Woo, K.C.; Wang, J.; Li, Q.; Sun, L.-D.; Zhang, X.; Lin, H.-Q.; Yan, C.H. Plasmonic percolation: Plasmon-manifested dielectric-to-metal transition. *ACS Nano* **2012**, *6*, 7162–7171. [\[CrossRef\]](#)
21. Karbovnyk, I.; Klym, H.; Chalyy, D.; Zhydenko, I.; Lukashevych, D. Impedance analysis of PEDOT: PSS/CNT composites below percolation threshold. *Appl. Nanosci.* **2022**, *12*, 1263–1266. [\[CrossRef\]](#)
22. Leong, E.S.P.; Wu, S.; Zhang, N.; Loh, W.W.; Khoo, E.H.; Si, G.Y.; Dai, H.T.; Liu, Y.J. Optical properties of ultrafine line and space polymeric nanogratings coated with metal and metal–dielectric–metal thin films. *Nanotechnology* **2014**, *25*, 055203. [\[CrossRef\]](#) [\[PubMed\]](#)
23. Hedl, E.; Bregović, V.B.; Rakić, I.Š.; Bergmann, A.; Sancho-Parramon, J. Evolution of optical properties of Au thin films with thermal annealing. *Opt. Mater.* **2024**, *150*, 115129. [\[CrossRef\]](#)
24. Cattin, L.; Jouad, E.; Stephant, N.; Louarn, G.; Morsli, M.; Hssein, M.; Mouchaal, Y.; Thoui, S.; Addou, M.; Khelil, A.; et al. Dielectric/metal/dielectric alternative transparent electrode: Observations on stability/degradation. *J. Phys. D Appl. Phys.* **2017**, *50*, 375502. [\[CrossRef\]](#)
25. Zhang, C.; Ji, C.; Park, Y.B.; Guo, L.J. Thin-metal-film-based transparent conductors: Material preparation, optical design, and device applications. *Adv. Opt. Mater.* **2021**, *9*, 2001298. [\[CrossRef\]](#)
26. Vafaei, M.; Moradi, M.; Bordbar, G.H. Realization of epsilon-near-zero metamaterial stack based on dielectric-semiconductor-metal multilayers. *Plasmonics* **2019**, *14*, 1929–1937. [\[CrossRef\]](#)
27. Pogosov, V.V. On the specific behavior of the work function and surface potential of an asymmetric metal-dielectric nanosandwich. *Low Temp. Phys.* **2024**, *50*, 342–349. [\[CrossRef\]](#)
28. Bolesta, I.; Velgosh, S.; Datsiuk, Y.; Karbovnyk, I.; Lesivtsiv, V.; Kulay, T.; Popov, A.I.; Bellucci, S.; Cestelli Guidi, M.; Marcelli, A. Optical, Infrared and Electron-Microscopy Studies of (Cd)<sub>n</sub> Metallic Clusters in Layered CdI<sub>2</sub> Crystals. *Radiat. Meas.* **2007**, *42*, 851–854. [\[CrossRef\]](#)
29. Bellucci, S.; Bolesta, I.; Guidi, M.C.; Karbovnyk, I.; Lesivtsiv, V.; Micciulla, F.; Pastore, R.; Popov, A.; Velgosh, S. Cadmium clusters in CdI<sub>2</sub> layered crystals: The influence on the optical properties. *J. Phys. Condens. Matter* **2007**, *19*, 395015. [\[CrossRef\]](#)
30. Cheng, Y.L.; Peng, W.F.; Huang, C.J.; Chen, G.S.; Fang, J.S. Reliability Characteristics of Metal-Insulator-Semiconductor Capacitors with Low-Dielectric-Constant Materials. *Molecules* **2023**, *28*, 1134. [\[CrossRef\]](#)

31. Yakovkin, I.; Reshetnyak, V. Controlling plasmon resonance of gold and silver nanoparticle arrays with help of liquid crystal. *Photonics* **2023**, *10*, 1088. [\[CrossRef\]](#)
32. Cueva, A.; Carretero, E. Comparison of the Optical Properties of Different Dielectric Materials (SnO<sub>2</sub>, ZnO, AZO, or SiAlN<sub>x</sub>) Used in Silver-Based Low-Emissivity Coatings. *Coatings* **2023**, *13*, 1709. [\[CrossRef\]](#)
33. Li, M.; Li, Y.; Zou, N.; Wu, J.; Wei, W.; Cao, G.; Yang, J. Optimizing the design of highly linearly polarized white LED with multilayer metal-dielectric grating structure. *Opt. Mater.* **2024**, *147*, 114684. [\[CrossRef\]](#)
34. Sardar, M.R.; Faisal, M. Numerical analysis of highly sensitive twin-core, gold-coated, D-shaped photonic crystal fiber based on surface plasmon resonance sensor. *Sensors* **2023**, *23*, 5029. [\[CrossRef\]](#) [\[PubMed\]](#)
35. Lu, L.; Luo, Z.; Xu, T.; Yu, L. Cooperative plasmonic effect of Ag and Au nanoparticles on enhancing performance of polymer solar cells. *Nano Lett.* **2013**, *13*, 59–64. [\[CrossRef\]](#)
36. Alkhalayfeh, M.A.; Aziz, A.A.; Pakhuruddin, M.Z.; Katubi, K.M.M. Plasmonic effects of Au@Ag nanoparticles in buffer and active layers of polymer solar cells for efficiency enhancement. *Materials* **2022**, *15*, 5472. [\[CrossRef\]](#) [\[PubMed\]](#)
37. Mitra, S.; Basak, M. Diverse bio-sensing and therapeutic applications of plasmon enhanced nanostructures. *Mater. Today* **2022**, *57*, 225–261. [\[CrossRef\]](#)
38. Badshah, M.A.; Koh, N.Y.; Zia, A.W.; Abbas, N.; Zahra, Z.; Saleem, M.W. Recent developments in plasmonic nanostructures for metal enhanced fluorescence-based biosensing. *Nanomaterials* **2020**, *10*, 1749. [\[CrossRef\]](#)
39. Alberti, G.; Zanon, C.; Magnaghi, L.R.; Biesuz, R. Gold and silver nanoparticle-based colorimetric sensors: New trends and applications. *Chemosensors* **2021**, *9*, 305. [\[CrossRef\]](#)
40. Prymaková, J.; Kaimlová, M.; Hubáček, T.; Švorčík, V.; Siegel, J. Nanostructured materials for artificial tissue replacements. *Int. J. Mol. Sci.* **2020**, *21*, 2521. [\[CrossRef\]](#)
41. Wei, H.; Eilers, H. From silver nanoparticles to thin films: Evolution of microstructure and electrical conduction on glass substrates. *J. Phys. Chem. Solids* **2009**, *70*, 459–465. [\[CrossRef\]](#)
42. Bolesta, I.M.; Borodchuk, A.V.; Kushnir, A.A.; Kolych, I.I.; Syworotka, I.I. Morphology and absorption spectra of ultra-thin films of silver. *J. Phys. Stud.* **2011**, *15*, 4703. [\[CrossRef\]](#)
43. Bolesta, I.; Kolych, I.; Kushnir, A.; Karbovnyk, I.; Collins, J.; Gamernyk, R.; Luchechko, A.; Rykhlyuk, S. Local fields in nanostructured silver films. *J. Nanophotonics* **2014**, *8*, 083087. [\[CrossRef\]](#)
44. Gwyddion. Available online: <https://gwyddion.net/> (accessed on 5 July 2024).
45. Lončarić, M.; Sancho-Parramon, J.; Pavlović, M.; Zorc, H.; Dubček, P.; Turkovic, A.; Bernstorff, S.; Jakopic, G.; Haase, A. Optical and structural characterization of silver island films on glass substrates. *Vacuum* **2009**, *84*, 188–192. [\[CrossRef\]](#)
46. Xu, G.; Tazawa, M.; Jin, P.; Nakao, S. Surface plasmon resonance of sputtered Ag films: Substrate and mass thickness dependence. *Appl. Phys. A* **2005**, *80*, 1535–1540. [\[CrossRef\]](#)
47. Bihun, R.I.; Stasyuk, Z.V.; Gavrylukh, M.V.; Leonov, D.S. Influence of Silicon Sublayers on the Optical Properties of Silver Thin Films. *Met. Adv. Technol.* **2019**, *41*, 1567–1574. [\[CrossRef\]](#)
48. Bihun, R.; Koman, B. *Nanoscale Metal Film Electronics. Traditions and New Scientific Strategies in the Context of Global Transformation of Society: Scientific Monograph*; Part 1. “Physical and mathematical sciences”; Baltija Publishing: Riga, Latvia, 2024; pp. 1–33. [\[CrossRef\]](#)
49. Lee, G.J.; Lee, Y.; Jung, B.-Y.; Jung, S.; Hwangbo, C.K.; Kim, J.; Yoon, C. Microstructural and Nonlinear Optical Properties of Thin Silver Films Near the Optical Percolation Threshold. *J. Korean Phys. Soc.* **2007**, *51*, 1555. [\[CrossRef\]](#)
50. Degarmo, E.P.; Black, J.; Kohser, R.A. *Materials and Processes in Manufacturing*, 9th ed.; Wiley: New York, NY, USA, 2003.
51. Lutter, L.; Serpell, C.; Tuite, M.; Serpell, L.; Xue, W.-F. Three-dimensional reconstruction of individual helical nano-filament structures from atomic force microscopy topographs. *Biomol. Concepts* **2020**, *11*, 102–115. [\[CrossRef\]](#)
52. Bellotti, R.; Picotto, G.B.; Ribotta, L. AFM Measurements and Tip Characterization of Nanoparticles with Different Shapes. *Nanomanufacturing Metrol.* **2022**, *5*, 127–138. [\[CrossRef\]](#)
53. Marques-Moros, F.; Forment-Aliaga, A.; Pinilla-Cienfuegos, E. Mirror effect in atomic force microscopy profiles enables tip reconstruction. *Sci. Rep.* **2020**, *10*, 18911. [\[CrossRef\]](#)
54. Arildsen, T.; Oxvig, C.S.; Pedersen, P.S.; Ostergaard, J.; Larsen, T. Reconstruction Algorithms in Undersampled AFM Imaging. *IEEE J. Sel. Top. Signal Process.* **2016**, *10*, 31–46. [\[CrossRef\]](#)
55. Liu, H.; Wang, B.; Leong, E.S.P.; Yang, P.; Zong, Y.; Si, G.; Maier, S.A. Enhanced Surface Plasmon Resonance on a Smooth Silver Film with a Seed Growth Layer. *ACS Nano* **2010**, *4*, 3139–3146. [\[CrossRef\]](#)
56. Liang, S.; Schwartzkopf, M.; Roth, S.V.; Müller-Buschbaum, P. State of the art of ultra-thin gold layers: Formation fundamentals and applications. *Nanoscale Adv.* **2022**, *4*, 2533–2560. [\[CrossRef\]](#) [\[PubMed\]](#)
57. Jardim, S.; António, J.; Mora, C. Graphical Image Region Extraction with K-Means Clustering and Watershed. *J. Imaging* **2022**, *8*, 163. [\[CrossRef\]](#)
58. Xu, X.; Xu, S.; Jin, L.; Song, E. Characteristic analysis of Otsu threshold and its applications. *Pattern Recognit. Lett.* **2011**, *32*, 956–961. [\[CrossRef\]](#)

59. Klym, H.; Kushnir, O.; Karbovnyk, I. Surface crystallization of GeSe<sub>2</sub> in the 80GeSe<sub>2</sub>–20Ga<sub>2</sub>Se<sub>3</sub> glasses caused by thermal annealing: Experimental study and statistical analysis. *Appl. Nanosci.* **2023**, *13*, 7445–7454. [[CrossRef](#)]
60. Zbilut, J.P.; Marwan, N. The Wiener–Khinchin theorem and recurrence quantification. *Phys. Lett. A* **2008**, *372*, 6622–6626. [[CrossRef](#)]
61. Gong, Y.; Misture, S.T.; Gao, P.; Mellott, N.P. Surface Roughness Measurements Using Power Spectrum Density Analysis with Enhanced Spatial Correlation Length. *J. Phys. Chem. C* **2016**, *120*, 22358–22364. [[CrossRef](#)]
62. Ifeachor, E.C.; Jervis, B.W. *Digital Signal Processing: A Practical Approach*; Pearson Education: London, UK, 2002.
63. Schroeder, M. *Fractals, Chaos, Power Laws: Minutes from an Infinite Paradise*; Courier Corporation: New York, NY, USA, 2009.

**Disclaimer/Publisher’s Note:** The statements, opinions and data contained in all publications are solely those of the individual author(s) and contributor(s) and not of MDPI and/or the editor(s). MDPI and/or the editor(s) disclaim responsibility for any injury to people or property resulting from any ideas, methods, instructions or products referred to in the content.